

**Responses to the comments on “Contrasting terrestrial
carbon cycle responses to the 1997/98 and 2015/16 extreme
El Niño events”**

Dear Referees and Editor,

Thank you very much for your efforts to deal with our manuscript and provide constructive comments. We have tried our best to re-summarize the results, and modify this manuscript accordingly. The following is our point-by-point reply to the comments.

Reply to Referee #2

The authors did a good job in revising their manuscript following the comments from the reviewers. The only suggestion I would have is corresponding to their revision - We have added a sentence. "Therefore, it is important to have clear insight into the impacts of ENSO events on the terrestrial carbon cycle, and this is best achieved through representative case studies." I feel that the first half of the sentence does not justify what this study is specially designed for, and is too general. I would suggest add "individual" between the "the impacts of" and "ENSO events".

In climate science, scientists have published review paper (A. Capotondi, A. T. Wittenberg, M. Newman, E. Di Lorenzo, J.-Y. Yu, P. Braconnot, J. Cole, B. Dewitte, B. Giese, E. Guilyardi, F.-F. Jin, K. Karnauskas, B. Kirtman, T. Lee, N. Schneider, Y. Xue, and S.-W. Yeh. Bulletin of the American Meteorological Society, 2015. DOI: 10.1175/BAMS-D-13-00117.1) on ENSO diversity and pointed out that each ENSO event is different from the other. I think what this review suggests clearly indicates the value and importance of studying how Carbon cycle responds to individual ENSO

events.

I would suggest accept with small amendments.

Reply: Thanks very much for your constructive suggestions. We have added the “individual” between the “the impacts of” and “ENSO events” in the context. Also, we have added this reference (Capotondi et al., 2015) into the text for illustrating the differences in F_{TA}/CO_2 CGR responses to different ENSO events, seen as “*we should keep in mind that the terrestrial carbon cycle responds in a unique way in terms of its strength, spatial patterns, biological processes, to every El Niño/La Niña event, because of the ENSO diversity with different spatial patterns and evolutions (Capotondi et al., 2015; Schwalm, 2011).*”

1 **Contrasting terrestrial carbon cycle responses to the 1997/98 and** 2 **2015/16 extreme El Niño events**

3 Jun Wang^{1,2}, Ning Zeng^{2,3}, Meirong Wang⁴, Fei Jiang¹, Hengmao Wang¹, and Ziqiang
4 Jiang¹

5 ¹International Institute for Earth System Science, Nanjing University, Nanjing, China

6 ²State Key Laboratory of Numerical Modelling for Atmospheric Sciences and Geophysical Fluid
7 Dynamics, Institute of Atmospheric Physics, Beijing, China

8 ³Department of Atmospheric and Oceanic Science and Earth System Science Interdisciplinary
9 Center, University of Maryland, College Park, Maryland, USA

10 ⁴~~Joint Center for Data Assimilation Research and Applications~~/Key Laboratory of Meteorological
11 Disaster of Ministry of Education, Nanjing University of Information Science & Technology,
12 Nanjing, China

13 Correspondence to: J. Wang (wangjun@nju.edu.cn)

15 **Abstract**

16 Large interannual atmospheric CO₂ variability is dominated by the response of the
17 terrestrial biosphere to El Niño–Southern Oscillation (ENSO). However, the behavior
18 of terrestrial ecosystems differs during different El Niños in terms of patterns and
19 biological processes. Here, we comprehensively compare two extreme El Niños
20 (2015/16 and 1997/98) in the context of a multi-event ‘composite’ El Niño. We find
21 large differences in the terrestrial carbon cycle responses, even though the two events
22 were of similar magnitude.

23
24 More specifically, we find that the global-scale land–atmosphere carbon flux (F_{TA})
25 anomaly during the 1997/98 El Niño was 1.64 Pg C yr⁻¹, but half that quantity during
26 the 2015/16 El Niño (at 0.73 Pg C yr⁻¹). Moreover, F_{TA} showed no obvious lagged

删除的内容: Collaborative Innovation Center on Forest and
Evaluation of Meteorological Disasters

29 response during the 2015/16 El Niño, in contrast to that during 1997/98. Separating the
30 global flux by geographical regions, the fluxes in the tropics and extratropical northern
31 hemisphere were 1.70 and $-0.05 \text{ Pg C yr}^{-1}$ during 1997/98, respectively. During
32 2015/16, they were 1.12 and $-0.52 \text{ Pg C yr}^{-1}$, respectively. Analysis of the mechanism
33 shows that, in the tropics, the widespread drier and warmer conditions caused a
34 decrease in gross primary productivity (GPP; $-0.73 \text{ Pg C yr}^{-1}$) and an increase in
35 terrestrial ecosystem respiration (TER; $0.62 \text{ Pg C yr}^{-1}$) during the 1997/98 El Niño. In
36 contrast, anomalously wet conditions occurred in the Sahel and East Africa during
37 2015/16, which caused an increase in GPP, compensating for its reduction in other
38 tropical regions. As a result, the total 2015/16 tropical GPP and TER anomalies were
39 -0.03 and $0.95 \text{ Pg C yr}^{-1}$. GPP dominance during 1997/98 and TER dominance during
40 2015/16 accounted for the phase difference in their F_{TA} . In the extratropical northern
41 hemisphere, the large difference occurred because temperatures over Eurasia were
42 warmer during the 2015/16, as compared with the cooling seen during the 1997/98 and
43 the composite El Niño. These warmer conditions enhanced GPP and TER over Eurasia
44 during the 2015/16 El Niño, while these fluxes were suppressed during 1997/98. The
45 total extratropical northern hemisphere GPP and TER anomalies were 0.63 and 0.55 Pg
46 C yr^{-1} during 1997/98, and 1.90 and 1.45 Pg C yr^{-1} during 2015/16, respectively.
47 Additionally, wildfires played a less important role during the 2015/16 than during the
48 1997/98 El Niño.

49

50

51

52

53

54 1 Introduction

55 The atmospheric CO₂ growth rate has significant interannual variability, greatly
56 influenced by the El Niño–Southern Oscillation (ENSO) (Bacastow, 1976; Keeling et
57 al., 1995). This interannual variability primarily stems from terrestrial ecosystems
58 (Bousquet et al., 2000; Zeng et al., 2005). There is also a general consensus that the
59 tropical terrestrial ecosystems account for the terrestrial carbon variability (Cox et al.,
60 2013; Peylin et al., 2013; Wang et al., 2016; Wang et al., 2013; Zeng et al., 2005). They
61 tend to release anomalous levels of carbon flux during El Niño episodes, and take up
62 carbon during La Niña events (Wang et al., 2016; Zeng et al., 2005). Recently, Ahlstrom
63 et al. (2015) further suggested that ecosystems in semi-arid regions dominated the
64 terrestrial carbon interannual variability, with a 39% contribution.

65 The terrestrial dominance primarily results from the drive-response mechanisms in
66 climate variability (especially in temperature and precipitation) caused by ENSO and
67 plant/soil physiology (Jung et al., 2017; Tian et al., 1998; Wang et al., 2016; Zeng et al.,
68 2005). The land–atmosphere carbon flux (F_{TA} – positive sign meaning a flux into the
69 atmosphere) can mainly be attributed to the imbalance between the gross primary
70 productivity (GPP) and terrestrial ecosystem respiration (TER) according to $F_{TA} \cong$
71 $TER - GPP + C_{fire}$, where the carbon flux from wildfires (C_{fire}) is generally much
72 smaller than the GPP or TER. Variations in each, or all, result in the changes in F_{TA} .

73 Based on a dynamical global vegetation model (DGVM), Zeng et al. (2005) found that
74 net primary productivity (NPP) contributed to almost three quarters of the tropical F_{TA}
75 interannual variability. Multi-model simulations involved in the TRENDY project and
76 CMIP5 have consistently suggested that NPP or GPP dominate the terrestrial carbon
77 variability (Ahlstrom et al., 2015; Kim et al., 2016; Piao et al., 2013; Wang et al., 2016).
78 These biological process analyses suggest that precipitation variation is the dominant

删除的内容: Therefore, v

80 climate factor in controlling F_{TA} interannual variability (Ahlstrom et al., 2015; Qian et
81 al., 2008; Tian et al., 1998; Wang et al., 2016; Zeng et al., 2005). Qian et al. (2008)
82 calculated the contributions of tropical precipitation and temperature as 56% and 44%,
83 respectively, based on model sensitivity experiments. Eddy covariance network
84 observations have suggested that the interannual carbon flux variability over tropical
85 and temperate regions is controlled by precipitation, while boreal ecosystem carbon
86 fluxes are more affected by temperature and radiation (Jung et al., 2011). At the same
87 time, there is a significant positive correlation between the atmospheric CO_2 growth
88 rate and mean tropical land temperature (Anderegg et al., 2015; Cox et al., 2013; Wang
89 et al., 2013; Wang et al., 2014). Regression analysis indicates an anomaly of
90 approximately 3.5 Pg C yr^{-1} in the CO_2 growth rate with a 1°C increase in tropical land
91 temperature, whereas a weaker interannual coupling exists between the CO_2 growth
92 rate and tropical land precipitation (Wang et al., 2013). Clark et al. (2003) and Doughty
93 et al. (2008) also concluded, based on in-situ observations, that warming anomalies can
94 reduce tropical tree growth and CO_2 uptake. Therefore, considering this strong
95 emergent linear relationship, these studies (Anderegg et al., 2015; Cox et al., 2013;
96 Clark et al., 2003; Doughty et al., 2008; Wang et al., 2013; Wang et al., 2014) have
97 suggested that temperature dominates the interannual variability of the F_{TA} or CO_2
98 growth rate. To reconcile these contradictory reports, Jung et al. (2017) showed that the
99 temporal and spatial compensatory effects in water availability link the yearly global
100 F_{TA} variability to temperature. Fang et al. (2017) suggested an ENSO-phase-dependent
101 interplay between water availability and temperature in controlling the tropical
102 terrestrial carbon cycle response to climate variability.

103 Apart from these long-term time series studies on the interannual F_{TA} or CO_2 growth
104 rate variability, we should keep in mind that the terrestrial carbon cycle responds in a

105 unique way in terms of its strength, spatial patterns, biological processes, to every El
106 Niño/La Niña event, because of the ENSO diversity with different spatial patterns and
107 evolutions (Capotondi et al., 2015; Schwalm, 2011). For example, wildfires played an
108 important role in the F_{TA} anomalies during the 1997/98 El Niño (van der Werf et al.,
109 2004). Therefore, it is important to have clear insight into the impacts of individual
110 ENSO events on the terrestrial carbon cycle, and this is best achieved through
111 representative case studies. Recently, one of the three extreme El Niño events in
112 recorded history occurred in 2015/16
113 (<https://www.esrl.noaa.gov/psd/enso/current.html>). Because of the interference of the
114 El Chichón eruption during the extreme El Niño case in 1982/83, we chose to compare
115 in detail the response of terrestrial ecosystems in the other two extreme El Niño events,
116 i.e., in 1997/98 and 2015/16, in the context of a multi-event ‘composite’ El Niño, based
117 on the VEGAS DGVM in its near-real-time framework and inversion datasets
118 [Copernicus Atmosphere Monitoring Service (CAMS), Monitoring Atmospheric
119 Composition & Climate (MACC), and CarbonTracker]. The purpose is to clarify the
120 different responses of biological processes in these two extreme events.
121 The paper is organized as follows: Section 2 describes the mechanistic carbon cycle
122 model used, its drivers, and reference datasets. Section 3 presents the results of the total
123 terrestrial carbon flux anomalies and spatial patterns, along with their mechanisms.
124 Finally, a discussion and concluding remarks are provided in Section 4.

125

126 **2 Model, datasets and Methods**

127 **2.1 Mechanistic carbon cycle model and its drivers**

128 We used the state-of-the-art VEGAS DGVM, version 2.4, in its near-real-time
129 framework, to investigate the responses of terrestrial ecosystems to El Niño events.

130 VEGAS has been widely used to study the terrestrial carbon cycle on its seasonal cycle,
131 interannual variability, and long-term trends (Zeng et al., 2005; Zeng et al., 2004; Zeng
132 et al., 2014). The model has also extensively participated in international carbon
133 modelling projects, such as the Coupled Climate–Carbon Cycle Model Intercomparison
134 Project (C⁴MIP; Friedlingstein et al., 2006), the TRENDY project (Sitch et al., 2015)
135 and the Multi-scale Synthesis and Terrestrial Model Intercomparison Project (MsTMIP;
136 Huntzinger et al., 2013). A detailed description of the model structure and biological
137 processes can be found in the appendix of Zeng et al. (2005). We ran VEGAS at the
138 0.5°×0.5° horizontal resolution from 1901 until the end of 2016, and focused on the
139 period from 1980 to 2016.

140 The climate fields and boundary forcings used to run VEGAS were:

- 141 (1) Precipitation datasets generated by combining the Climatic Research Unit (CRU)
142 Time-series (TS) Version 3.22 (University of East Anglia Climatic Research Unit et al.,
143 2014), NOAA’s Precipitation Reconstruction over Land (PREC/L) (Chen et al., 2002),
144 and the NOAA–NCEP Climate Anomaly Monitoring System-Outgoing Longwave
145 Radiation Precipitation Index (CAMS-OPI) (Janowiak and Xie, 1999).
- 146 (2) Temperature data from the CRU TS3.22 before the year 2013, and generated by
147 combining the CRU 1981–2010 climatology and the Goddard Institute for Space
148 Studies (GISS) Surface Temperature Analysis (GISTEMP) (Hansen et al., 2010) after
149 2013.
- 150 (3) Downward shortwave radiation from the driver datasets in MsTMIP (Wei et al.,
151 2014) before 2010, with the value of the year 2010 repeated for subsequent years.
- 152 (4) The gridded cropland and pasture land use datasets integrated from the History
153 Database of the Global Environment (HYDE) (Klein Goldewijk et al., 2011) with an
154 linear extrapolation in 2016.

删除的内容:)

删除的内容: (

删除的内容: force

带格式的: 字体:(默认) Times New Roman

158

159 **2.2 Reference datasets**

160 We selected a series of reference datasets to compare to the VEGAS simulation. The
161 atmospheric CO₂ concentrations were from the monthly in-situ CO₂ datasets at the
162 Mauna Loa Observatory, Hawaii (Keeling et al., 1976). The Niño 3.4 (120°W–170°W,
163 5°S–5°N) sea surface temperature anomaly (SSTA) data were from the NOAA’s
164 Extended Reconstructed Sea Surface Temperature (ERSST) dataset, version 4 (Huang
165 et al., 2015), with a three-month running average. We compared the CAMS (1980–
166 2015) and MACC (1980–2014) inversion results (Chevallier, 2013) and the
167 CarbonTracker2016 (2000–2015) with the CarbonTracker near-real time results from
168 2016 (Peters et al., 2007) with VEGAS. The F_{TA} in CarbonTracker was calculated by
169 the sum of the posterior biospheric flux and its imposed fire emissions. The Satellite-
170 based fire emissions were from the Global Fire Emissions Database, Version 4
171 (GFEDv4) from 1997 through 2014 (Randerson et al., 2015). Owing to the high
172 correlation between the solar-induced chlorophyll fluorescence (SIF) and terrestrial
173 GPP (Guanter et al., 2014), we selected the monthly satellite SIF from the GOME2_F
174 version 26 from 2007 to 2016 (Joiner et al., 2012). We also compared the Enhanced
175 Vegetation Index (EVI) from MODIS MOD13C2 (Didan, 2015) with the simulated leaf
176 area index (LAI) anomalies.

177

178 **2.4 Methods**

179 To calculate the anomalies during the El Niño events, we first removed the long-term
180 climatology in each dataset for getting rid of seasonal cycle signals. We then detrended
181 them based on the linear regression, because the trend was mainly caused by long-term
182 CO₂ fertilization and climate change. We used these detrended monthly anomalies to

183 investigate the impacts of El Niño events on the terrestrial carbon cycle.

184

185 **3 Results**

186 **3.1 Total terrestrial carbon flux anomalies**

187 Three extreme El Niño events (1982/83, 1997/98, and 2015/16) occurred from 1980 to
188 2016, with their maximum SSTAs above 2.0 K (Fig. 1a). An El Niño event tends to
189 anomalously increase the atmospheric CO₂ growth rate (Fig. 1b); therefore, there are
190 two significant anomalous increases in CO₂ growth rate that correspond to the 1997/98
191 and 2015/16 El Niño events, although the maximum increase in 2015/16 was slightly
192 less than that in 1997/98. Because of the diffuse light disturbance (Mercado et al., 2009)
193 of the Mount El Chichón eruption during the 1982/83 El Niño on the canonical coupling
194 between the anomalies of the CO₂ growth rate anomalies and El Niño events, we mainly
195 focused on the 1997/98 and 2015/16 El Niño events in this study. The interannual
196 variability of the atmospheric CO₂ growth rate principally originates from the terrestrial
197 ecosystems (Fig. 1c). The correlation coefficient between the CO₂ growth rate
198 anomalies and the global F_{TA} simulated by VEGAS was 0.60 ($p < 0.05$). In order to
199 evaluate the performance of the VEGAS simulation on the interannual time scale, we
200 also present CAMS, MACC and CarbonTracker inversion results. The CAMS and
201 MACC inversions were nearly the same, with a correlation coefficient of approximately
202 0.60 ($p < 0.05$) with VEGAS. From 2000 to 2016, CarbonTracker was highly correlated
203 with VEGAS ($r = 0.67$, $p < 0.05$). These high correlation coefficients between VEGAS
204 and the reference datasets indicate that VEGAS can capture the terrestrial carbon cycle
205 interannual variability well.

206 There were 10 El Niño events from 1980 to 2016, each with a different duration and
207 strength (Table 1). According to the definition of El Niño, these 10 events can be

208 categorized into two weak (with a 0.5 to 0.9 SSTA), three moderate (1.0 to 1.4), two
209 strong (1.5 to 1.9), and three very strong (≥ 2.0) events. During the 1997/98 El Niño,
210 the positive SSTA lasted from April 1997 to June 1998, while the positive SSTA
211 occurred in winter 2014, and extended to June 2016 in the 2015/16 El Niño (Fig. 2a).
212 However, every El Niño event always peaks in winter (November or December; Fig.
213 2a). Considering this phase-lock phenomenon in the El Niño events, we produced a
214 composite analysis (excluding 1982/83 and 1991/92, because of the diffuse radiation
215 disturbances) as the background responses of the terrestrial carbon cycle to El Niño
216 events.

217 The evolution of the [global](#) F_{TA} anomalies in VEGAS, the mean of CAMS and MACC,
218 and CarbonTraker in the composite, 1997/98, and 2015/16 El Niño events, are closely
219 consistent with the Mauna Loa CGR anomalies (Figs. 2b–d). The peaks of the F_{TA} and
220 the Mauna Loa CGR anomalies in the 1997/98 and 2015/16 El Niño events were much
221 stronger than those in the composite analysis. Importantly, there were significant
222 terrestrial lagged responses in the composite and 1997/98 El Niño events, with the peak
223 of the F_{TA} anomaly occurring from March to April in the El Niño decaying year (Figs.
224 2b and c), consistent with previous studies (Qian et al., 2008; Wang et al., 2016).
225 However, this lagged terrestrial response disappeared in the Mauna Loa CGR, VEGAS
226 and CarbonTracker in the 2015/16 El Niño (Fig. 2d). In June 2016, the F_{TA} anomaly of
227 VEGAS and CarbonTracker reduced significantly (the sign changed), whereas the
228 Mauna Loa CGR reduced only slightly (no sign change; Fig. 2d). A similar
229 phenomenon also occurred earlier, from April to July 2015. In addition, the anomalous
230 carbon release caused by the El Niño lasted from approximately July in the El Niño
231 developing year to October in the El Niño decaying year (Figs. 2b–d). For simplicity,
232 we calculated the total anomalies of all El Niño events during this period in the next

233 context, taking the terrestrial lagged responses into account (Wang et al., 2016).
234 Based on the major geographical regions, we separated global F_{TA} anomaly into the
235 extratropical northern hemisphere ($23^{\circ}N-90^{\circ}N$), tropical regions ($23^{\circ}S-23^{\circ}N$), and
236 extratropical southern hemisphere ($60^{\circ}S-23^{\circ}S$). Because the F_{TA} anomaly over the
237 extratropical southern hemisphere is generally smaller, we mainly present the
238 evolutions of the F_{TA} over the extratropical northern hemisphere and the tropical regions
239 in Fig. 3. Comparing the global and tropical F_{TA} anomalies, the F_{TA} anomalies in the
240 tropical regions dominated the global F_{TA} during these El Niño events (Figs. 3b, d and
241 f), in accordance with previous conclusions (Peylin et al., 2013; Zeng et al., 2005). The
242 F_{TA} anomalies over the extratropical northern hemisphere were nearly neutral in
243 VEGAS for the composite and the 1997/98 El Niño events (Figs. 3a and c). However,
244 there was clear anomalous uptake from April to September in 2016 simulated by
245 VEGAS (Fig. 3e), compensating for the carbon release over the tropics (Fig. 3f). This
246 anomalous uptake caused the globally negative F_{TA} anomalies that occurred from May
247 to September in 2016 (Fig. 2d). Similar anomalous uptake also occurred over the
248 extratropical northern hemisphere from April to July 2015. This anomalous uptake in
249 VEGAS was to some extent consistent with the results from CarbonTracker, and
250 accounted for the global F_{TA} reduction mentioned above during these periods.
251 Comparing the behaviors between the Mauna Loa CGR and the F_{TA} anomalies, the
252 Mauna Loa CGR, which originates from a tropical observatory, does not reflect the
253 signals over the extratropical northern hemisphere in time (Figs. 2d and 3e).
254 Because F_{TA} mainly stems from the difference between TER and GPP, we present the
255 TER and GPP anomalies in Fig. 4 to clearly explain the F_{TA} anomalies. Anomalous
256 negative GPP dominated the F_{TA} anomaly in the tropics in the composite and the
257 1997/98 El Niño episodes, with the significant lagged responses (peak at approximately

258 May of the El Niño decaying year; Figs. 4b and d). Furthermore, clear positive TER
259 anomalies occurred from October 1997 to April 1998 (Fig. 4d), contributing to the
260 tropical carbon release during this period (Fig. 3d). In contrast, anomalously positive
261 TER dominated the F_{TA} anomaly in the tropics during the 2015/16 El Niño, without
262 clear lags (Fig. 4f), accounting for the disappearance of the terrestrial F_{TA} lagged
263 response (Fig. 2d). In the extratropical northern hemisphere, the increased GPP and
264 TER from April to October were nearly identical in the composite and in 1998 (Figs.
265 4a and c), causing neutral F_{TA} anomalies (Figs. 3a and c). However, the increased GPP
266 was stronger than the increased TER from April to July 2015 and from April to
267 September 2016 (Fig. 4e), resulting in the anomalous uptake in F_{TA} (Figs. 2d and 3e).
268 We calculated the total carbon flux anomalies from July in the El Niño developing year
269 to October in the El Niño decaying year. The composite global F_{TA} anomaly during the
270 El Niño events in VEGAS was approximately $0.60 \text{ Pg C yr}^{-1}$, dominated by tropical
271 ecosystems with $0.61 \text{ Pg C yr}^{-1}$ (Table 2). These anomalies were comparable to the
272 mean of the CAMS and MACC inversion results, at 0.92 ± 0.01 globally and 0.66 ± 0.03
273 Pg C yr^{-1} in the tropics. In these two extreme cases, a strong anomalous carbon release
274 occurred during the 1997/98 El Niño, with a value of $1.64 \text{ Pg C yr}^{-1}$, which was less
275 than the $2.57 \text{ Pg C yr}^{-1}$ in the CAMS and MACC inversions; while only $0.73 \text{ Pg C yr}^{-1}$
276 was released during the 2015/16 El Niño, which was comparable to the $0.82 \text{ Pg C yr}^{-1}$
277 in CarbonTracker. However, the F_{TA} anomalies in the tropical regions dominated the
278 global F_{TA} anomalies in both cases, with values of 1.70 and $1.12 \text{ Pg C yr}^{-1}$ in VEGAS,
279 respectively. Furthermore, anomalous carbon uptake simulated by VEGAS over the
280 extratropical northern hemisphere cancelled out the $0.52 \text{ Pg C yr}^{-1}$ anomalous release
281 in the tropics during the 2015/16 El Niño, whereas it was neutral ($-0.05 \text{ Pg C yr}^{-1}$) in
282 the 1997/98 El Niño. The F_{TA} anomaly was relatively smaller in the extratropical

283 southern hemisphere.

284 In terms of the biological processes, the GPP ($-0.73 \text{ Pg C yr}^{-1}$) and TER (0.62 Pg C
285 yr^{-1}) in the tropics together drove the anomalous F_{TA} during 1997/98, while the TER
286 ($0.95 \text{ Pg C yr}^{-1}$) mainly drove the anomalous F_{TA} during 2015/16, with a near neutral
287 GPP of $-0.03 \text{ Pg C yr}^{-1}$ (Table 2). These data confirmed that the GPP played a more
288 important role in the 1997/98 event, while TER was dominant during the 2015/16 El
289 Niño. In the extratropical northern hemisphere, GPP and TER cancelled each other out.
290 They were 0.13 and $0.08 \text{ Pg C yr}^{-1}$ in the composite analysis, and 0.63 and 0.55 Pg C
291 yr^{-1} in the 1997/98 El Niño, respectively, causing the near neutral F_{TA} anomaly in that
292 region. However, the GPP and TER in the 2015/16 El Niño were much stronger than
293 those in the composite or the 1997/98 El Niño. Importantly, the GPP ($1.90 \text{ Pg C yr}^{-1}$)
294 was stronger than the TER ($1.45 \text{ Pg C yr}^{-1}$) in the 2015/16 El Niño, causing the
295 significant carbon uptake. The F_{TA} anomaly caused by wildfires also played an
296 important role during the 1997/98 El Niño, with a global value of $0.42 \text{ Pg C yr}^{-1}$ in
297 VEGAS, which was consistent with the GFED fire data product ($0.82 \text{ Pg C yr}^{-1}$). The
298 effect of wildfires on the F_{TA} anomaly during the 1997/98 El Niño episode has been
299 previously suggested by van der Werf et al. (2004), whereas it was close to zero (0.05
300 Pg C yr^{-1}) during the 2015/16 El Niño.

301

302 **3.2 Spatial features and its mechanisms**

303 The regional responses of terrestrial ecosystems to El Niño events are inhomogeneous,
304 principally due to the anomalies in climate variability. In the composite El Niño analysis
305 (Fig. 5a), land consistently released carbon flux in the tropics, while there was an
306 anomalous carbon uptake over the North America as well as the central and eastern
307 Europe. These regional responses were generally consistent with the CAMS and

308 MACC inversion results (Fig. 5d).

309 During the 1997/98 El Niño episode, the tropical responses were analogous to the
310 composite results, except for stronger carbon releases. North America and central and
311 eastern China had stronger carbon uptake, whereas Europe and Russia had stronger
312 carbon release (Fig. 5b). However, during the 2015/16 El Niño, anomalous carbon
313 uptake occurred over the Sahel and East Africa, compensating for the carbon release
314 over the other tropical regions (Fig. 5c). This made the total F_{TA} anomaly in the tropics
315 in 2015/16 less than that in 1997/98 (Figs. 3d and f; and Table 2). North America had
316 anomalous carbon uptake, similar to that in the composite and the 1997/98 El Niño,
317 while central and eastern Russia had anomalous carbon uptake during the 2015/16 El
318 Niño (Fig. 5c), which was opposite to the carbon release in the composite and the
319 1997/98 El Niño. This opposite behavior of the boreal forests over the central and
320 eastern Russia clearly contributed to the total uptake over the extratropical northern
321 hemisphere (Table 2). Moreover, these regional responses during the 2015/16 El Niño
322 were significantly consistent with the CarbonTracker result (Fig. 5f).

323 To better explain these regional carbon flux anomalies, we present the main climate
324 variabilities of soil wetness (mainly caused by precipitation) and air temperature, and
325 the biological processes of GPP and TER in Fig. 6. In the composite analyses, the soil
326 wetness is generally reduced in the tropics (Fig. 6a), causing the widespread decrease
327 in GPP (Fig. 6b), which has been verified by model sensitivity experiments (Qian et al.,
328 2008). At the same time, air temperature was anomalously warmer, contributing to the
329 increase in TER. However, the drier conditions in the semi-arid regions, such as the
330 Sahel, South Africa, and Australia, restricted this increase in TER induced by warmer
331 temperatures (Fig. 6d). Higher air temperatures over the North America largely
332 enhanced the GPP and TER, while cooler conditions over the Eurasia reduced them

333 (Figs. 6b–d). Wetter conditions over parts of North America and Eurasia also increased
334 the GPP and TER to some extent (Fig. 6a).

335 Comparing the composite results (Figs. 6a–d) and the 1997/98 El Niño (Figs.6e–h), the
336 regional patterns were almost identical, except for the difference in magnitude. In
337 contrast, there were some differences in the 2015/16 El Niño. Over the Sahel and East
338 Africa, the soil wetness increased due to the higher precipitation (Fig. 6i), dynamically
339 cooling the air temperature (Fig. 6k). These wetter conditions largely benefit GPP (Fig.
340 6j), compensating for the reduced GPP over the other tropical regions. This caused GPP
341 near neutral in the tropics, as compared to the composite and the 1997/98 El Niño (Table
342 2). Higher soil moisture also contributed to increased TER over the Sahel (Fig. 6l),
343 contrary to that in the 1997/98 El Niño (Fig. 6h). This spatial compensation in GPP,
344 together with the widespread increase in TER, accounted for the TER dominance in the
345 tropics during the 2015/16 El Niño. Furthermore, the higher GPP resulted in the
346 anomalous carbon uptake in that region (Fig. 5c), which partly compensated for the
347 anomalous carbon release over the other tropical regions. This in part caused the smaller
348 tropical F_{TA} during the 2015/16 El Niño compared with that during 1997/98. Another
349 clear difference occurred over the Eurasia, with almost opposite signals during the
350 1997/98 and 2015/16 El Niño events. During the 2015/16 El Niño over the Eurasia, air
351 temperature was anomalously higher compared with the cooling in the composite and
352 during the 1997/98 El Niño (Figs. 6c, g, and k). This warmth enhanced the GPP and
353 TER (Figs. 6j and l), as compared with the reduced levels in the composite and during
354 the 1997/98 El Niño (Figs. 6b, d, f, and h). This phenomenon explains the stronger GPP
355 and TER anomalies, and the anomalous carbon uptake over the whole of the
356 extratropical northern hemisphere (Table 2).

357 Recently, more attention has been paid to SIF as an effective indicator of GPP (Guanter

358 et al., 2014). Therefore, we compared the simulated GPP and SIF variabilities on the
359 interannual time scale. Although noisy signals in SIF occurred, it was anomalously
360 positive over the USA, parts of Europe, and East Africa, and negative over the Amazon
361 and South Asia, during the 2015/16 El Niño, corresponding to increased and decreased
362 GPP, respectively (Figs. 7a and c). The match over other regions was not significant. In
363 addition, MODIS EVI increased anomalously over the North America, southern South
364 America, parts of Europe, the Sahel, and East Africa, but reduced over the Amazon,
365 northern Canada, central Africa, South Asia, and northern Australia (Fig. 7d). These
366 EVI anomalies corresponded well with the simulated LAI anomalies (Fig. 7b). The
367 good match between the simulated GPP (LAI) and SIF (EVI) gives us more confidence
368 in the VEGAS simulations.

369 Finally, wildfires, as important disturbances for F_{TA} , always release carbon flux.
370 Although the F_{TA} anomalies caused by wildfires were generally smaller than the GPP
371 or TER anomalies, they played an important role during the 1997/98 El Niño (globally,
372 $0.42 \text{ Pg C yr}^{-1}$ in VEGAS and $0.82 \text{ Pg C yr}^{-1}$ in GFED; Table 2), which is consistent
373 with previous work (van der Werf et al., 2004). The F_{TA} anomalies caused by wildfires
374 are shown in Fig. 8. The correlation coefficients between the simulated global F_{TA}
375 anomalies caused by wildfires and the GFED fire data product was 0.46 (unsmoothed)
376 and 0.63 (smoothed; Fig. 8a), confirming that VEGAS has certain capability in
377 simulating this disturbance. During the 1997/98 El Niño, satellite-based GFED data
378 show that the F_{TA} anomalies caused by wildfires mainly occurred over the tropical
379 regions, such as the Amazon, central Africa, South Asia, and Indonesia (Fig. 8d).
380 VEGAS also simulated the positive F_{TA} over these tropical regions (Fig. 8b). The total
381 tropical F_{TA} anomalies caused by fires were $0.37 \text{ Pg C yr}^{-1}$ in VEGAS and 0.72 Pg C
382 yr^{-1} in GFED (Table 2). During the 2015/16 El Niño, wildfires also resulted in positive

383 F_{TA} anomalies over the Amazon, South Asia, and Indonesia; however, their magnitudes
384 were smaller than those during the 1997/98 El Niño, because it was much drier during
385 the 1997/98 event than the 2015/16 one (Figs. 6e and i). In addition, the wetter
386 conditions over East Africa during the 2015/16 El Niño suppressed the occurrences of
387 wildfires with the negative F_{TA} anomalies (Fig. 8c). The total tropical F_{TA} anomaly was
388 $0.11 \text{ Pg C yr}^{-1}$ in VEGAS (Table 2). Therefore, wildfires played a less important role
389 during the 2015/16 event than during the 1997-98 one. The F_{TA} anomalies caused by
390 wildfires over the extratropics were much weaker than those over the tropics, and the
391 match between VEGAS and GFED was poorer (Table 2; Figs. 8b and d).

392

393 **4 Conclusions and Discussion**

394 The magnitudes and patterns of climate anomalies caused by different El Niño events
395 differ. Therefore, the responses of terrestrial carbon cycle to different El Niño episodes
396 remain uncertain (Schwalm, 2011). In this study, we compared in detail the impacts of
397 two extreme El Niño events in recorded history (namely, the recent 2015/16, and earlier
398 1997/98 events) on the terrestrial carbon cycle in the context of a multi-event
399 ‘composite’ El Niño. We used VEGAS in its near-real-time framework, along with
400 inversion datasets. The main conclusions can be summarized as follows:

401 (1) The simulations indicated that the global-scale F_{TA} anomaly during the 2015/16 El
402 Niño was $0.73 \text{ Pg C yr}^{-1}$, which was nearly two times smaller than that during the
403 1997/98 El Niño ($1.64 \text{ Pg C yr}^{-1}$), and was confirmed by the inversion results. The
404 F_{TA} had no obvious lagged response during the 2015/16 El Niño, in contrast to that
405 during the 1997/98 El Niño. Separating the global fluxes, the fluxes in the tropics
406 and the extratropical northern hemisphere were 1.12 and $-0.52 \text{ Pg C yr}^{-1}$ during
407 the 2015/16 El Niño, respectively, whereas they were 1.70 and $-0.05 \text{ Pg C yr}^{-1}$

408 during the 1997/98 event. Tropical F_{TA} anomalies dominated the global F_{TA}
409 anomalies during both extreme El Niño events.

410 (2) Mechanistic analysis indicates that anomalously wet conditions occurred over the
411 Sahel and East Africa during the 2015/16 El Niño, resulting in the increase in GPP,
412 which compensated for the reduction in GPP over the other tropical regions. In total,
413 this caused a near neutral GPP in the tropics ($-0.03 \text{ Pg C yr}^{-1}$), compared with the
414 composite analysis ($-0.54 \text{ Pg C yr}^{-1}$) and the 1997/98 El Niño ($-0.73 \text{ Pg C yr}^{-1}$).
415 The spatial compensation in GPP and the widespread increase in TER (0.95 Pg C
416 yr^{-1}) explained the dominance of TER during the 2015/16 El Niño, compared with
417 the GPP dominance during the 1997/98 event. The different biological dominance
418 accounted for the phase difference in the F_{TA} responses during the 1997/98 and
419 2015/16 El Niño events.

420 (3) Higher air temperatures over North America largely enhanced the GPP and TER
421 during the 1997/98 and 2015-16 El Niño events. However, the air temperatures
422 during the 2015/16 El Niño over the Eurasia were anomalously higher, compared
423 with the cooling during the 1997/98 El Niño episode. These warmer conditions
424 benefited the GPP and TER, accounting for the stronger GPP ($1.90 \text{ Pg C yr}^{-1}$) and
425 TER ($1.45 \text{ Pg C yr}^{-1}$) anomalies and anomalous carbon uptake ($-0.52 \text{ Pg C yr}^{-1}$)
426 over the extratropical northern hemisphere during the 2015/16 El Niño.

427 (4) Wildfires, frequent in the tropics, played an important role in the F_{TA} anomalies
428 during the 1997/98 El Niño episode, confirmed by the VEGAS simulation and the
429 satellite-based GFED fire product. However, the VEGAS simulation showed that
430 the tropical F_{TA} caused by wildfires during the 2015/16 El Niño was relatively
431 smaller than that during the 1997/98 El Niño. This result was mainly because the
432 tropical weather was much drier during the 1997/98 event than during the 2015-16

433 one.

434 It is important to keep in mind that the responses of the terrestrial carbon cycle to the
435 El Niño events in this study were simulated using an individual DGVM (VEGAS),
436 which, whilst highly consistent with the variations in the CGR and inversion results,
437 carries uncertainties in terms of the regional responses because of, for example, its
438 model structure, biological processes considered, and parameterizations. Of course,
439 uncertainties exist in all of the state-of-the-art DGVMs. Fang et al. (2017) recently
440 suggested that none of the 10 contemporary terrestrial biosphere models captures the
441 ENSO-phase-dependent responses. If possible, we will quantify the inter-model
442 uncertainties in regional responses of the terrestrial carbon cycle to El Niño events
443 when the new round of TRENDY simulations (1901–2016) becomes available.
444 Although we used three inversion datasets as reference for the VEGAS simulation in
445 this study, they cover different periods. Importantly, there are also large uncertainties
446 between the different atmospheric CO₂ inversions because of their different prescribed
447 priors, *a priori* uncertainties, inverse methods, and observational datasets (Peylin et al.,
448 2013). Future atmospheric CO₂ inversions may produce more accurate results based on
449 more observational datasets, including surface and satellite-based observations.

450 Recently, more studies have pointed out that the 1997/98 El Niño evolved following
451 the eastern Pacific El Niño dynamics, which depends on basin-wide thermocline
452 variations, whereas the 2015/16 event involves additionally the central Pacific El Niño
453 dynamics that relies on the subtropical forcing (Paek et al., 2017; Palmeiro et al., 2017).
454 Therefore, it is necessary to investigate the different impacts of the eastern and central
455 Pacific El Niño types (Ashok et al., 2007) on the terrestrial carbon cycle in the future.
456 This may give us an additional insight into the contrasting responses of the terrestrial
457 carbon cycle to the 1997/98 and 2015/16 El Niño events. We believe that doing so will

458 contribute greatly to deepening our knowledge of present and future carbon cycle
459 variations on the interannual time scales.

460

461 **Data Availability**

462 In this study, all the datasets can be freely accessed. The Mauna Loa monthly CO₂
463 records are available at <https://www.esrl.noaa.gov/gmd/ccgg/trends/data.html>. The
464 ERSST4 Niño3.4 index can be accessed from

465 <http://www.cpc.ncep.noaa.gov/data/indices/ersst4.nino.mth.81-10.ascii>. The CAMS

466 and MACC inversions are available at <http://apps.ecmwf.int/datasets/>. The

467 CarbonTracker datasets can be found at

468 <https://www.esrl.noaa.gov/gmd/ccgg/carbontracker/>. The GFEDv4 global fire

469 emissions are downloaded at https://daac.ornl.gov/cgi-bin/dsviewer.pl?ds_id=1293.

470 Satellite SIF datasets are retrieved from

471 http://avdc.gsfc.nasa.gov/pub/data/satellite/MetOp/GOME_F/MetOp-A/level3/.

472 MODIS enhanced vegetation index (EVI) datasets are downloaded from

473 https://lpdaac.usgs.gov/dataset_discovery/modis/modis_products_table/mod13c2_v00

474 [6](#).

475

476 **Acknowledgements:**

477 We gratefully acknowledge the ESRL for the use of their Mauna Loa atmospheric CO₂

478 records and CarbonTracker datasets; NOAA for the ERSST4 ENSO index; LSCE-IPSL

479 for the CAMS and MACC inversion datasets; the Oak Ridge National Laboratory

480 Distributed Active Archive Center for the GFEDv4 global fire emissions; NASA

481 Goddard Space Flight Center for the SIF datasets; and the Land Processes Distributed

482 Active Archive Center for the MODIS EVI datasets. This study was supported by the

483 National Key R&D Program of China (Grant No. 2016YFA0600204 [and No.](#)
484 [2017YFB0504000](#)) and the Natural Science Foundation for Young Scientists of Jiangsu
485 Province, China (Grant No. BK20160625).

486

487 **References**

488 Ahlstrom, A., Raupach, M. R., Schurgers, G., Smith, B., Arneeth, A., Jung, M.,
489 Reichstein, M., Canadell, J. G., Friedlingstein, P., Jain, A. K., Kato, E., Poulter, B.,
490 Sitch, S., Stocker, B. D., Viovy, N., Wang, Y. P., Wiltshire, A., Zaehle, S., and Zeng, N.:
491 The dominant role of semi-arid ecosystems in the trend and variability of the land CO₂
492 sink, *Science*, 348, 895-899, 2015.

493 Anderegg, W. R., Ballantyne, A. P., Smith, W. K., Majkut, J., Rabin, S., Beaulieu, C.,
494 Birdsey, R., Dunne, J. P., Houghton, R. A., Myneni, R. B., Pan, Y., Sarmiento, J. L.,
495 Serota, N., Shevliakova, E., Tans, P., and Pacala, S. W.: Tropical nighttime warming as
496 a dominant driver of variability in the terrestrial carbon sink, *Proc Natl Acad Sci U S*
497 *A*, 112, 15591-15596, 2015.

498 Ashok, K., Behera, S. K., Rao, S. A., Weng, H., and Yamagata, T.: El Niño Modoki and
499 its possible teleconnection, *J. Geophys. Res.*, 112, C11007, 2007.

500 Bacastow, R. B.: Modulation of atmospheric carbon dioxide by the Southern Oscillation,
501 *Nature*, 261, 116-118, 1976.

502 Bousquet, P., Peylin, P., Ciais, P., Le Quere, C., Friedlingstein, P., and Tans, P. P.:
503 Regional changes in carbon dioxide fluxes of land and oceans since 1980, *Science*, 290,
504 1342-1346, 2000.

505 [Capotondi, A., Wittenberg, A. T., Newman, M., Lorenzo, E. Di, Yu, J. Y., Braconnot,](#)
506 [P., Cole, J., Dewitte, B., Giese, B., Guilyardi, E., Jin, F. F., Karnauskas, K., Kirtman,](#)
507 [B., Lee, T., Schneider, N., Xue, Y., and Yeh, S. W.: Understanding ENSO diversity,](#)

508 [Bulletin of the American Meteorological Society, 96, 921-938, 2015.](#)
509 Chen, M., Xie, P., Janowiak, J. E., and Arkin, P. A.: Global Land Precipitation: A 50-yr
510 Monthly Analysis Based on Gauge Observations, *Journal of Hydrometeorology*, 3, 249-
511 266, 2002.
512 Chevallier, F.: On the parallelization of atmospheric inversions of CO₂ surface fluxes
513 within a variational framework, *Geosci Model Dev*, 6, 783-790, 2013.
514 Clark, D. A., Piper, S. C., Keeling, C. D., and Clark, D. B.: Tropical rain forest tree
515 growth and atmospheric carbon dynamics linked to interannual temperature variation
516 during 1984-2000, *P. Natl. Acad. Sci. USA*, 100, 5852-5857, 2003.
517 Cox, P. M., Pearson, D., Booth, B. B., Friedlingstein, P., Huntingford, C., Jones, C. D.,
518 and Luke, C. M.: Sensitivity of tropical carbon to climate change constrained by carbon
519 dioxide variability, *Nature*, 494, 341-344, 2013.
520 Didan, K.: MOD13C2 MODIS/Terra Vegetation Indices Monthly L3 Global 0.05Deg
521 CMG V006. NASA EOSDIS Land Processes DAAC.
522 <https://doi.org/10.5067/MODIS/MOD13C2.006>, 2015.
523 Doughty, C. E., and Goulden, M. L.: Are tropical forests near a high temperature
524 threshold?, *J. Geophys. Res.*, 113, G00B07, 2008.
525 Fang, Y., Michalak, A. M., Schwalm, C. R., Huntzinger, D. N., Berry, J. A., Ciais, P.,
526 Piao, S. L., Poulter, B., Fisher, J. B., Cook, R. B., Hayes, D., Huang, M. Y., Ito, A., Jain,
527 A., Lei, H. M., Lu, C. Q., Mao, J. F., Parazoo, N. C., Peng, S. S., Ricciuto, D. M., Shi,
528 X. Y., Tao, B., Tian, H. Q., Wang, W. L., Wei, Y. X., and Yang, J.: Global land carbon
529 sink response to temperature and precipitation varies with ENSO phase, *Environ. Res.*
530 *Lett.*, 12, 064007, 2017.
531 Friedlingstein, P., Cox, P., Betts, R., Bopp, L., Von Bloh, W., Brovkin, V., Cadule, P.,
532 Doney, S., Eby, M., Fung, I., Bala, G., John, J., Jones, C., Joos, F., Kato, T., Kawamiya,

533 M., Knorr, W., Lindsay, K., Matthews, H. D., Raddatz, T., Rayner, P., Reick, C.,
534 Roeckner, E., Schnitzler, K. G., Schnur, R., Strassmann, K., Weaver, A. J., Yoshikawa,
535 C., and Zeng, N.: Climate-carbon cycle feedback analysis: Results from the C⁴MIP
536 model intercomparison, *Journal of Climate*, 19, 3337-3353, 2006.

537 Guanter, L., Zhang, Y. G., Jung, M., Joiner, J., Voigt, M., Berry, J. A., Frankenberg, C.,
538 Huete, A. R., Zarco-Tejada, P., Lee, J. E., Moran, M. S., Ponce-Campos, G., Beer, C.,
539 Camps-Valls, G., Buchmann, N., Gianelle, D., Klumpp, K., Cescatti, A., Baker, J. M.,
540 and Griffis, T. J.: Global and time-resolved monitoring of crop photosynthesis with
541 chlorophyll fluorescence, *PNAS*, doi: 0.1073/pnas.1320008111, 2014. E1327–E1333,
542 2014.

543 Hansen, J., Ruedy, R., Sato, M., and Lo, K.: Global Surface Temperature Change,
544 *Reviews of Geophysics*, 48, 2010.

545 Huang, B., Banzon, V. F., Freeman, E., Lawrimore, J., Liu, W., Peterson, T. C., Smith,
546 T. M., Thorne, P. W., Woodruff, S. D., and Zhang, H.-M.: Extended Reconstructed Sea
547 Surface Temperature Version 4 (ERSST.v4). Part I: Upgrades and Intercomparisons,
548 *Journal of Climate*, 28, 911-930, 2015.

549 Huntzinger, D. N., Schwalm, C., Michalak, A. M., Schaefer, K., King, A. W., Wei, Y.,
550 Jacobson, A., Liu, S., Cook, R. B., Post, W. M., Berthier, G., Hayes, D., Huang, M., Ito,
551 A., Lei, H., Lu, C., Mao, J., Peng, C. H., Peng, S., Poulter, B., Ricciuto, D., Shi, X.,
552 Tian, H., Wang, W., Zeng, N., Zhao, F., and Zhu, Q.: The North American Carbon
553 Program Multi-Scale Synthesis and Terrestrial Model Intercomparison Project – Part 1:
554 Overview and experimental design, *Geosci Model Dev*, 6, 2121-2133, 2013.

555 Janowiak, J. E. and Xie, P.: CAMS-OPI: A Global Satellite-Rain Gauge Merged
556 Product for Real-Time Precipitation Monitoring Applications, *J. Clim.*, 12, 3335-3342,
557 1999.

558 Joiner, J., Yoshida, Y., Vasilkov, A. P., Middleton, E. M., Campbell, P. K. E., Yoshida,
559 Y., Kuze, A., and Corp, L. A.: Filling-in of near-infrared solar lines by terrestrial
560 fluorescence and other geophysical effects: simulations and space-based observations
561 from SCIAMACHY and GOSAT, *Atmospheric Measurement Techniques*, 5, 809-829,
562 2012.

563 Jung, M., Reichstein, M., Margolis, H. A., Cescatti, A., Richardson, A. D., Arain, M.
564 A., Arneth, A., Bernhofer, C., Bonal, D., Chen, J. Q., Gianelle, D., Gobron, N., Kiely,
565 G., Kutsch, W., Lasslop, G., Law, B. E., Lindroth, A., Merbold, L., Montagnani, L.,
566 Moors, E. J., Papale, D., Sottocornola, M., Vaccari, F., and Williams, C.: Global patterns
567 of land-atmosphere fluxes of carbon dioxide, latent heat, and sensible heat derived from
568 eddy covariance, satellite, and meteorological observations, *J Geophys Res-Bioge*,
569 116, 2011.

570 Jung, M., Reichstein, M., Schwalm, C. R., Huntingford, C., Sitch, S., Ahlstrom, A.,
571 Arneth, A., Camps-Valls, G., Ciais, P., Friedlingstein, P., Gans, F., Ichii, K., Jain, A. K.,
572 Kato, E., Papale, D., Poulter, B., Raduly, B., Rodenbeck, C., Tramontana, G., Viovy,
573 N., Wang, Y. P., Weber, U., Zaehle, S., and Zeng, N.: Compensatory water effects link
574 yearly global land CO₂ sink changes to temperature, *Nature*, 541, 516-520, 2017.

575 Keeling, C. D., Bacastow, R. B., Bainbridge, A. E., Ekdahl, C. A., Guenther, P. R.,
576 Waterman, L. S., and Chin, J. F. S.: Atmospheric Carbon-Dioxide Variations at Mauna-
577 Loa Observatory, Hawaii, *Tellus*, 28, 538-551, 1976.

578 Keeling, C. D., Whorf, T. P., Wahlen, M., and Vanderpligt, J.: Interannual Extremes in
579 the Rate of Rise of Atmospheric Carbon-Dioxide since 1980, *Nature*, 375, 666-670,
580 1995.

581 Kim, J. S., Kug, J. S., Yoon, J. H., and Jeong, S. J.: Increased atmospheric CO₂ growth
582 rate during El Niño driven by reduced terrestrial productivity in the CMIP5 ESMs,

583 *Journal of Climate*, 29, 8783-8805, 2016.

584 Klein Goldewijk, K., Beusen, A., Van Drecht, G., and De Vos, M.: The HYDE 3.1
585 spatially explicit database of human-induced global land-use change over the past
586 12,000 years, *Global Ecology and Biogeography*, 20, 73-86, 2011.

587 Mercado, L. M., Bellouin, N., Sitch, S., Boucher, O., Huntingford, C., Wild, M., and
588 Cox, P. M.: Impact of changes in diffuse radiation on the global land carbon sink, *Nature*,
589 458, 1014-U1087, 2009.

590 Paek, H., Yu, J.-Y., and Qian, C.: Why were the 2015/16 and 1997/1998 extreme El
591 Niño different?, *Geophys. Res. Lett.*, 44, 18848-18856, 2017.

592 Palmeiro, F. M., Iza, M., Barriopedro, D., Calvo, N., and Garcia-Herrera, R.: The
593 complex behavior of El Niño winter 2015-2016, *Geophys. Res. Lett.*, 44, 2902-2910,
594 2017.

595 Peters, W., Jacobson, A. R., Sweeney, C., Andrews, A. E., Conway, T. J., Masarie, K.,
596 Miller, J. B., Bruhwiler, L. M., Petron, G., Hirsch, A. I., Worthy, D. E., van der Werf,
597 G. R., Randerson, J. T., Wennberg, P. O., Krol, M. C., and Tans, P. P.: An atmospheric
598 perspective on North American carbon dioxide exchange: CarbonTracker, *Proc Natl*
599 *Acad Sci U S A*, 104, 18925-18930, 2007.

600 Peylin, P., Law, R. M., Gurney, K. R., Chevallier, F., Jacobson, A. R., Maki, T., Niwa,
601 Y., Patra, P. K., Peters, W., Rayner, P. J., Rödenbeck, C., van der Laan-Luijkx, I. T., and
602 Zhang, X.: Global atmospheric carbon budget: results from an ensemble of atmospheric
603 CO₂ inversions, *Biogeosciences*, 10, 6699-6720, 2013.

604 Piao, S., Sitch, S., Ciais, P., Friedlingstein, P., Peylin, P., Wang, X., Ahlström, A., Anav,
605 A., Canadell, J. G., Cong, N., Huntingford, C., Jung, M., Levis, S., Levy, P. E., Li, J.,
606 Lin, X., Lomas, M. R., Lu, M., Luo, Y., Ma, Y., Myneni, R. B., Poulter, B., Sun, Z.,
607 Wang, T., Viovy, N., Zaehle, S., and Zeng, N.: Evaluation of terrestrial carbon cycle

608 models for their response to climate variability and to CO₂ trends, *Global Change*
609 *Biology*, doi: 10.1111/gcb.12187, 2013. 2117–2132, 2013.

610 Qian, H., Joseph, R., and Zeng, N.: Response of the terrestrial carbon cycle to the El
611 Nino-Southern Oscillation, *Tellus Series B-Chemical and Physical Meteorology*, 60,
612 537-550, 2008.

613 Randerson, J. T., van der Werf, G. R., Giglio, L., Collatz, G. J. and Kasibhatla, P.
614 S.:Global Fire Emissions Database, Version 4, (GFEDv4). ORNL DAAC, Oak Ridge,
615 Tennessee, USA. <http://dx.doi.org/10.3334/ORNLDAAC/1293>, 2015.

616 Schwalm, C. R.: Does terrestrial drought explain global CO₂ flux anomalies induced
617 by El Nino?, *Biogeosciences*, 8, 2493-2506, 2011.

618 Sitch, S., Friedlingstein, P., Gruber, N., Jones, S. D., Murray-Tortarolo, G., Ahlström,
619 A., Doney, S. C., Graven, H., Heinze, C., Huntingford, C., Levis, S., Levy, P. E., Lomas,
620 M., Poulter, B., Viovy, N., Zaehle, S., Zeng, N., Arneeth, A., Bonan, G., Bopp, L.,
621 Canadell, J. G., Chevallier, F., Ciais, P., Ellis, R., Gloor, M., Peylin, P., Piao, S. L., Le
622 Quéré, C., Smith, B., Zhu, Z., and Myneni, R.: Recent trends and drivers of regional
623 sources and sinks of carbon dioxide, *Biogeosciences*, 12, 653-679, 2015. Tian, H. Q.,
624 Melillo, J. M., Kicklighter, D. W., McGuire, A. D., Helfrich, J. V. K., Moore, B., and
625 Vorosmarty, C. J.: Effect of interannual climate variability on carbon storage in
626 Amazonian ecosystems, *Nature*, 396, 664-667, 1998.

627 University of East Anglia Climatic Research Unit, Harris, I.C., Jones, P.D.: CRU
628 TS3.22: Climatic Research Unit (CRU) Time-Series (TS) Version 3.22 of High
629 Resolution Gridded Data of Month-by-month Variation in Climate (Jan. 1901- Dec.
630 2013). NCAS British Atmospheric Data Centre, 2014.

631 van der Werf, G. R., Randerson, J. T., Collatz, G. J., Giglio, L., Kasibhatla, P. S.,
632 Arellano, A. F., Jr., Olsen, S. C., and Kasischke, E. S.: Continental-scale partitioning of

633 fire emissions during the 1997 to 2001 El Nino/La Nina period, *Science*, 303, 73-76,
634 2004.

635 Wang, J., Zeng, N., and Wang, M.: Interannual variability of the atmospheric CO₂
636 growth rate: roles of precipitation and temperature, *Biogeosciences*, 13, 2339-2352,
637 2016.

638 Wang, W., Ciais, P., Nemani, R., Canadell, J. G., Piao, S., Sitch, S., White, M. A.,
639 Hashimoto, H., Milesi, C., and Myneni, R. B.: Variations in atmospheric CO₂ growth
640 rates coupled with tropical temperature, *PNAS*, 110, 13061-13066, 2013.

641 Wang, X., Piao, S., Ciais, P., Friedlingstein, P., Myneni, R. B., Cox, P., Heimann, M.,
642 Miller, J., Peng, S., Wang, T., Yang, H., and Chen, A.: A two-fold increase of carbon
643 cycle sensitivity to tropical temperature variations, *Nature*, 506, 212-215, 2014.

644 Wei, Y., Liu, S., Huntzinger, D. N., Michalak, A. M., Viovy, N., Post, W. M., Schwalm,
645 C. R., Schaefer, K., Jacobson, A. R., Lu, C., Tian, H., Ricciuto, D. M., Cook, R. B.,
646 Mao, J., and Shi, X.: The North American Carbon Program Multi-scale Synthesis and
647 Terrestrial Model Intercomparison Project – Part 2: Environmental driver data, *Geosci*
648 *Model Dev*, 7, 2875-2893, 2014.

649 Zeng, N., Mariotti, A., and Wetzal, P.: Terrestrial mechanisms of interannual CO₂
650 variability, *Global Biogeochemical Cycles*, 19, GB1016, 2005.

651 Zeng, N., Qian, H. F., Munoz, E., and Iacono, R.: How strong is carbon cycle-climate
652 feedback under global warming?, *Geophys Res Lett*, 31, 2004.

653 Zeng, N., Zhao, F., Collatz, G. J., Kalnay, E., Salawitch, R. J., West, T. O., and Guanter,
654 L.: Agricultural Green Revolution as a driver of increasing atmospheric CO₂ seasonal
655 amplitude, *Nature*, 515, 394-397, 2014.

656

657

658

659

660

661

662 **Tables and Figures:**

663 **Table 1** Lists of El Niño events from 1980 till 2016.

No.	El Niño Events	Duration (months)	Maximum Nino3.4 Index (°C)
1	Apr1982–Jun1983	15	2.1
2	Sep1986–Feb1988	18	1.6
3	Jun1991–Jul1992	14	1.6
4	Oct1994–Mar1995	6	1.0
5	May1997–May1998	13	2.3
6	Jun2002–Feb2003	9	1.2
7	Jul2004–Apr2005	10	0.7
8	Sep2006–Jan2007	5	0.9
9	Jul2009–Apr2010	10	1.3
10	Nov2014–May2016	19	2.3

664

665 **Table 2** Carbon flux anomalies during El Niño events, calculated as the mean from July
666 in the El Niño developing year to October in the El Niño decaying year. Flux units are
667 in Pg C yr⁻¹.

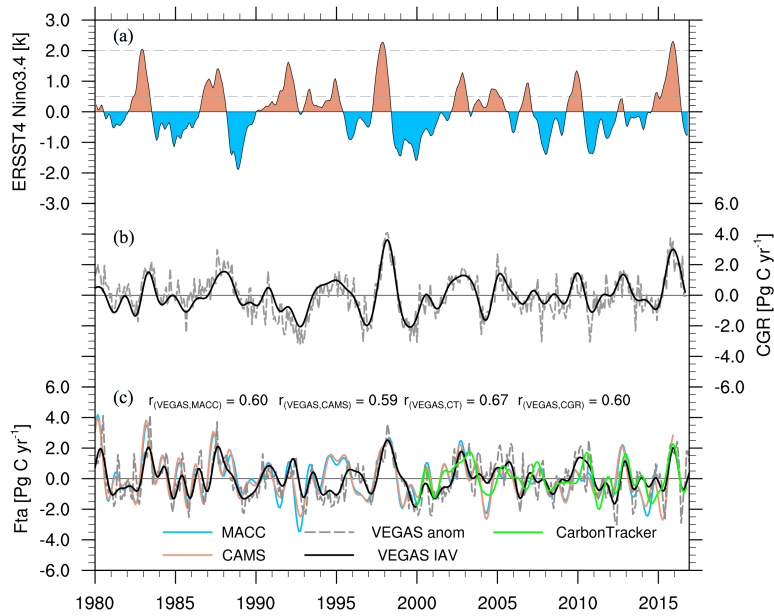
Zones	El Niños	Inversions		VEGAS Model				GFED
		F _{TA} (CAMS+MACC) ^a	F _{TA} (CarbonTracker)	F _{TA}	GPP	TER	C _{fire}	C _{fire}
Global	composite ^b	0.92±0.01	–	0.60	–0.55	–0.08	0.14	–

	1997/98	2.57±0.04	–	1.64	–0.04	1.28	0.42	0.82
	2015/16	–	0.82	0.73	1.59	2.24	0.05	–
	composite	0.20±0.02	–	–0.06	0.13	0.08	–0.01	–
NH	1997/98	0.40±0.07	–	–0.05	0.63	0.55	0.04	0.11
	2015/16	–	0.18	–0.52	1.90	1.45	–0.06	–
	composite	0.66±0.03	–	0.61	–0.54	–0.07	0.15	–
Tropical	1997/98	2.12±0.14	–	1.70	–0.73	0.62	0.37	0.72
	2015/16	–	0.53	1.12	–0.03	0.95	0.11	–
	composite	0.07±0.01	–	0.05	–0.14	–0.09	0.00	–
SH	1997/98	0.05±0.02	–	–0.02	0.14	0.12	0.00	–0.01
	2015/16	–	0.11	0.14	–0.28	–0.16	0.00	–

668 ^arepresents the mean value of the CAMS and MACC inversion results with the
669 uncertainty of their standard deviation.

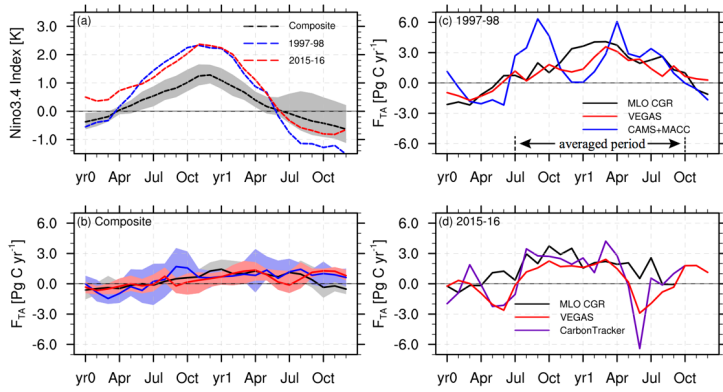
670 ^bComposite analyses exclude the 1982/83, 1991/92, and 2015/16 El Niño events,
671 because the former two cases were disturbed by the El Chichón and Pinatubo eruptions,
672 and the latter is not covered by the inversion datasets.

673



674

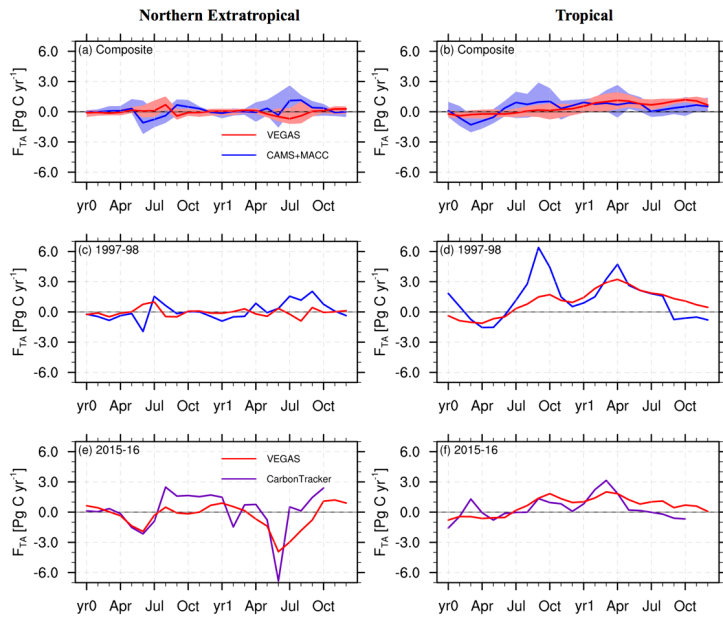
675 **Figure 1.** Interannual variability (IAV) in the sea surface temperature anomaly (SSTA)
 676 and carbon cycle. (a) ERSST4 Niño3.4 Index (units: K) using the 3-month running
 677 averaged SSTA for the Niño 3.4 region (5°N–5°S, 120°–170°W). (b) IAV in the Mauna
 678 Loa CO₂ growth rate (CGR; units: Pg C yr⁻¹). The CGR is calculated as the difference
 679 between the monthly mean in adjacent years. The dashed line is the detrended monthly
 680 anomaly and the solid line is smoothed by the butterworth filtering. (c) IAV in the land–
 681 atmosphere carbon fluxes (F_{TA} ; units: Pg C yr⁻¹). The blue and orange solid lines are
 682 the smoothed results of the MACC and CAMS inversions, respectively. The gray
 683 dashed line is the detrended anomaly and the black one is the smoothed result from the
 684 VEGAS model simulation. The green solid line is the smoothed CarbonTracker result.
 685



686

687 **Figure 2.** Evolutions of the global F_{TA} along with the development of El Niño. (a) the
 688 SSTa in the composite (black), 1997/98 (blue), and 2015/16 (red) El Niño events. (b)
 689 The F_{TA} anomalies in the El Niño composite analysis. The black solid line denotes the
 690 Mauna Loa CGR; and the red and blue lines show the VEGAS and mean of the CAMS
 691 and MACC inversions, respectively. The shaded areas in (a) and (b) show the 95%
 692 confidence intervals of the variables in the composite, derived in 1000 bootstrap
 693 estimates. (c) The F_{TA} anomalies during the 1997/98 El Niño events. The arrows
 694 demonstrate the time periods during which we calculate the carbon flux anomalies
 695 listed/presented in the table and figures. (d) The F_{TA} anomalies during the 2015/16 El
 696 Niño. The purple line denotes the result of the CarbonTracker2016 and CarbonTracker
 697 near-real-time datasets.

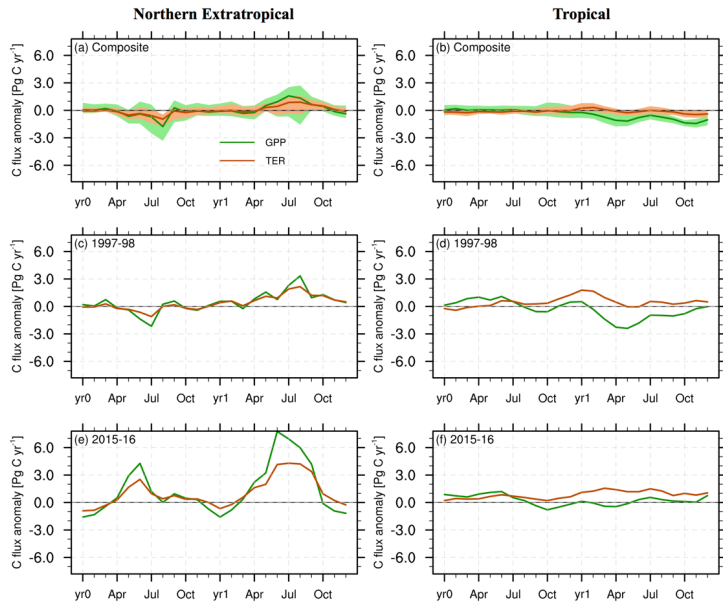
698



699

700 **Figure 3.** Evolutions of F_{TA} over the extratropical northern hemisphere (23°N – 90°N)
 701 and tropical regions (23°S – 23°N) along with the development of El Niño. (a, b)
 702 Composite results with the VEGAS simulation (red solid line) and the mean of the
 703 CAMS and MACC inversions (blue solid line). The shaded areas show the 95%
 704 confidence intervals of the variables in the composite, derived in 1000 bootstrap
 705 estimates. (c, d) The F_{TA} anomalies during the 1997/98 El Niño. (e, f) The F_{TA}
 706 anomalies in the 2015/16 El Niño with VEGAS (red solid line) and CarbonTracker
 707 (purple solid line).

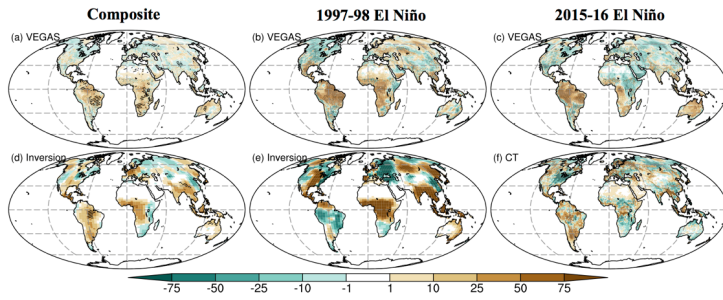
708



709

710 **Figure 4.** Evolutions of gross primary productivity (GPP, green lines) and terrestrial
 711 ecosystem respiration (TER, brown lines) over the extratropical northern hemisphere
 712 (23°N–90°N) and tropical regions (23°S–23°N) along with the development of El Niño.
 713 (a, b) El Niño composite results. The shaded areas show the 95% confidence intervals
 714 of the variables in the composite, derived in 1000 bootstrap estimates. (c, d) Results of
 715 the 1997/98 El Niño. (e, f) Results of the 2015/16 El Niño.

716



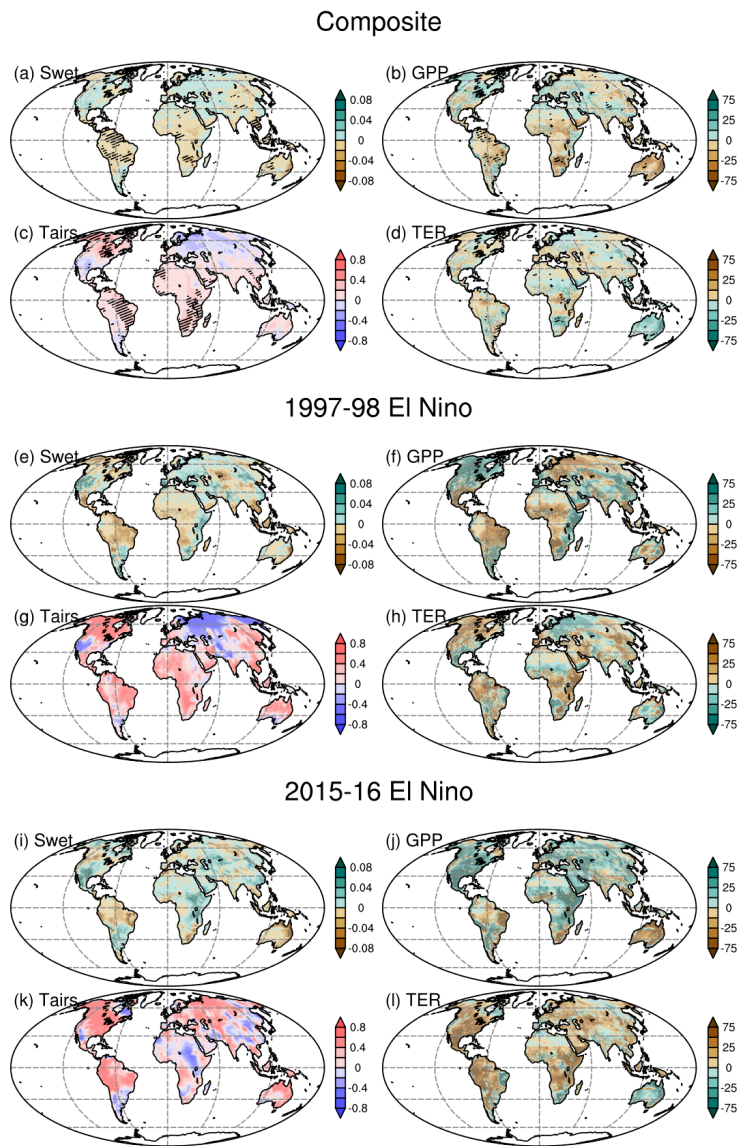
717

718 **Figure 5.** Spatial F_{TA} anomalies calculated from July in the El Niño developing year to
 719 October in the El Niño decaying year (units: $\text{g C m}^{-2} \text{yr}^{-1}$). (a–c) Results of the
 720 composite, 1997/98, and 2015/16 El Niño events simulated by VEGAS, respectively.
 721 (d–e) The averaged results of CAMS and MACC in the composite and 1997/98 El
 722 Niños. (f) The 2015/16 El Niño F_{TA} anomaly in CarbonTracker. The stippled areas in
 723 (a) and (d) are significant above the 90% level, estimated by Student’s t -test.

724

725

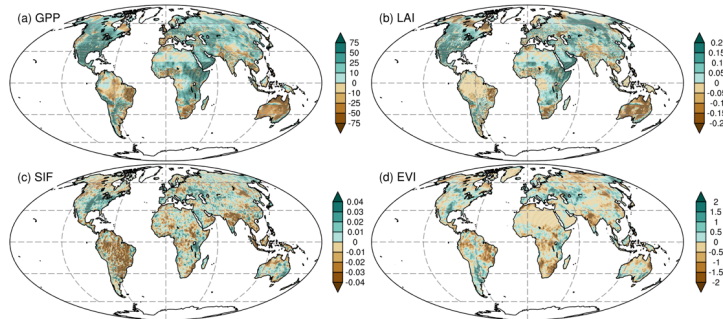
726



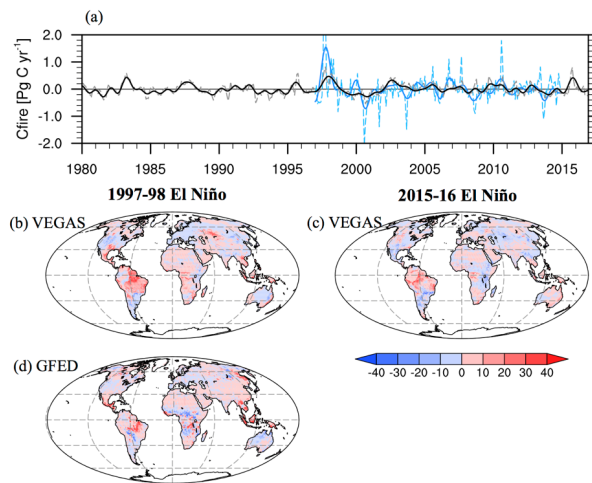
727

728 **Figure 6.** Anomalies of soil wetness, air temperature (units: K), GPP ($\text{g C m}^{-2} \text{ yr}^{-1}$),
 729 and TER ($\text{g C m}^{-2} \text{ yr}^{-1}$) from July in the El Niño developing year to October in the El
 730 Niño decaying year in the composite, 1997/98, and 2015/16 El Niño episodes,

731 respectively. (a–d) Results of the composite analyses. The stippled areas are significant
732 above the 90% levels estimated by the Student’s *t*-test. (e–h) Anomalies during the
733 1997/98 El Niño. (i–l) Anomalies during the 2015/16 El Niño.
734



735
736 **Figure 7.** Spatial anomalies in (a) the simulated GPP by VEGAS (units: $\text{g C m}^{-2} \text{yr}^{-1}$),
737 (b) the simulated leaf area index (LAI, units: $\text{m}^2 \text{m}^{-2}$), (c) solar-induced chlorophyll
738 fluorescence (SIF, units: $\text{mW m}^{-2} \text{nm}^{-1} \text{sr}^{-1}$), and (d) MODIS enhanced vegetation
739 index (EVI, $\times 10^{-2}$) from July 2015 to October 2016.
740



741
 742 **Figure 8.** F_{TA} anomalies induced by wildfires. (a) Total global anomalies (Pg C yr^{-1}).
 743 The dashed gray and solid black lines represent the anomalies simulated by VEGAS,
 744 detrended and smoothed by Butterworth filtering, respectively. The dashed and solid
 745 blue lines represent the GFED results. (b) Spatial F_{TA} anomaly ($\text{g C m}^{-2} \text{yr}^{-1}$) during
 746 the 1997/98 El Niño in VEGAS. (c) Spatial F_{TA} anomaly during the 2015/16 El Niño
 747 in VEGAS. (d) GFED anomaly during the 1997/98 El Niño episode.

748

749